

Article

Synthesis and Improved Photoluminescence of SnF₂-Derived CsSnCl₃-SnF₂:Mn²⁺ Perovskites via Rapid Thermal Treatment

Jisheng Xu, Haixia Wu, Xinye Lu, Yaqian Huang, Jianni Chen, Wendi Zhou, Zewen Lin , Jie Song, Hongliang Li * and Rui Huang *

School of Materials Science and Engineering, Hanshan Normal University, Chaozhou 521041, China; jishengxu2023@126.com (J.X.); 20220063@hstc.edu.cn (H.W.); lu15768524048@126.com (X.L.); h15976709657@126.com (Y.H.); a1963638106@126.com (J.C.); a54495597@126.com (W.Z.); zewenlin@126.com (Z.L.); songjie@hstc.edu.cn (J.S.)

* Correspondence: lhl4@hstc.edu.cn (H.L.); rhuang@hstc.edu.cn (R.H.)

Abstract: We report a rapid synthesis method for producing CsSnCl₃:Mn²⁺ perovskites, derived from SnF₂, and investigate the effects of rapid thermal treatment on their photoluminescence properties. Our study shows that the initial CsSnCl₃:Mn²⁺ samples exhibit a double luminescence peak structure with PL peaks at approximately 450 nm and 640 nm, respectively. These peaks originate from defect-related luminescent centers and the 4T¹→6A¹ transition of Mn²⁺. However, as a result of rapid thermal treatment, the blue emission is significantly reduced and the red emission intensity is increased nearly twofold compared to the pristine sample. Furthermore, the Mn²⁺-doped samples demonstrate excellent thermal stability after the rapid thermal treatment. We suggest that this improvement in photoluminescence results from enhanced excited-state density, energy transfer between defects and the Mn²⁺ state, as well as the reduction of nonradiative recombination centers. Our findings provide valuable insights into the luminescence dynamics of Mn²⁺-doped CsSnCl₃ and open up new possibilities for controlling and optimizing the emission of rare-earth-doped CsSnCl₃.

Keywords: CsSnCl₃; Mn²⁺; photoluminescence; rapid thermal treatment; SnF₂-derived



Citation: Xu, J.; Wu, H.; Lu, X.; Huang, Y.; Chen, J.; Zhou, W.; Lin, Z.; Song, J.; Li, H.; Huang, R. Synthesis and Improved Photoluminescence of SnF₂-Derived CsSnCl₃-SnF₂:Mn²⁺ Perovskites via Rapid Thermal Treatment. *Materials* **2023**, *16*, 4027. <https://doi.org/10.3390/ma16114027>

Academic Editor: Matthias Auf der Maur

Received: 4 May 2023
Revised: 25 May 2023
Accepted: 25 May 2023
Published: 28 May 2023



Copyright: © 2023 by the authors. Licensee MDPI, Basel, Switzerland. This article is an open access article distributed under the terms and conditions of the Creative Commons Attribution (CC BY) license (<https://creativecommons.org/licenses/by/4.0/>).

1. Introduction

In recent years, all-inorganic lead halide perovskite (CsPbX₃, X=Cl, Br, I) has garnered significant attention in optoelectronic devices due to its outstanding photoelectric properties, such as high photoluminescent quantum yield (PLQY), excellent defect tolerance, and tunable light emission [1–4]. Currently, LED devices based on CsPbX₃ have surpassed 20% external quantum efficiency. Further, the stability issues related to lead-based perovskites have been effectively improved via packaging, increasing their lifespan from a few hours to hundreds of hours. However, the high toxicity of lead poses a threat to human health and the ecological environment, thereby impeding their practical use. Therefore, there is a rising demand for non-toxic or less toxic elements to replace lead, such as equivalent substitution (Sn²⁺, Ge²⁺) and isovalent substitution (Bi³⁺, Ag⁺) to form lead-free perovskite luminescent materials [5–10]. It is proposed to replace Pb in lead-halide perovskite with divalent Sn and Ge cations as they both satisfy the prerequisites for coordination and charge balance. Sn²⁺ has an ion radius comparable to Pb²⁺ (1.35 Å for Sn²⁺ and 1.49 Å for Pb²⁺), resulting in the avoidance of significant lattice vibration caused by substitution. Additionally, Sn²⁺ possesses a similar ns² electronic configuration to Pb²⁺, making it possible to form a perovskite with the formula ASnX₃, akin to lead-based counterparts [11–17]. However, the formation energy of defects in Sn-based perovskites is relatively low (~250 meV), making it easy to form a defect density of up to 10¹⁹ cm⁻³ in Sn-based perovskites, which results in a PLQY of as low as 0.14% in these Sn-based perovskites. Additionally, Sn²⁺ is susceptible to oxidation into Sn⁴⁺ in air, leading to structural instability of perovskites and luminescence quenching.

Recently, Zhang et al. employed SnF_2 instead of easily oxidized SnBr_2 as a tin source and effectively improved the structural stability of Cs_4SnBr_6 perovskite through introducing F to inhibit the oxidation of Sn^{2+} in tin-based perovskite [18]. Despite the progress, the luminescence stability of cesium tin chloride perovskite is still poor, and the luminescence efficiency is too low to meet the application requirements. In particular, the synthesis and photoluminescence properties of SnF_2 -derived cesium–tin perovskite ($\text{CsSnCl}_3\text{-SnF}_2$) have not been reported so far.

On the other hand, impurity doping is considered an effective method to improve the luminescence properties and stability of tin-based perovskites. For instance, Dawson et al. successfully improved the stability of tin-based perovskites through replacing Sn^{2+} sites with Mn^{2+} [19]. Similarly, Hou et al. discovered that Mn^{2+} doping could improve the electron energy level structure and stability of tin halide perovskites and also greatly enhance the luminescence efficiency of $\text{CsSnCl}_3\text{:Mn}^{2+}$ to around 2% [20]. However, the low-temperature chemical synthesis of Mn-doped tin-based perovskites complicates the full activation of the Mn^{2+} luminescent centers. Due to tin-based halide perovskite materials' poor thermal stability, conventional thermal annealing may not effectively activate the Mn ion luminescent centers in this kind of material. Rapid thermal treatment (RTT), a transient process that is characterized by rapid heating and cooling, provides an alternative way to thermally activate the Mn ion luminescent centers of tin-based perovskites. Here, we describe a rapid synthesis method for SnF_2 -derived $\text{CsSnCl}_3\text{:Mn}^{2+}$ and investigate the effect of RTT on the photoluminescent (PL) properties of $\text{CsSnCl}_3\text{:Mn}^{2+}$ perovskites. Pristine $\text{CsSnCl}_3\text{:Mn}^{2+}$ displays a double luminescence peak structure, which includes PL peaks at around 450 nm and 640 nm, respectively. These peaks originate from defect-related luminescent centers and the $4T^1 \rightarrow 6A^1$ transition of Mn^{2+} , respectively. We found that RTT significantly reduced the blue emission and increased the red emission intensity nearly twofold compared to the pristine sample. Furthermore, the Mn^{2+} -doped samples exhibited excellent thermal stability after RTT processing. We discuss the improved PL based on our analysis of PL excitation spectra, XRD patterns, and PL decay traces.

2. Materials and Methods

Mn^{2+} -doped CsSnCl_3 were synthesized using a water-assisted wet ball-milling method. The reactant precursors included cesium chloride (4 mmol, CsCl, Aladdin, 99.9%), stannous fluoride (1 mmol, SnF_2 , Macklin, 99.9%), ammonium bromide (1 mmol, NH_4Cl , Aladdin, 99.99%), and manganous chloride (MnCl_2 , Macklin, 99%). To obtain Mn^{2+} -doped CsSnCl_3 with different levels, the molar ratios of CsCl, SnF_2 , and NH_4Cl were maintained at 1:1:2 mmol, whereas the molar ratio of MnCl_2 was kept at 1 mmol. Firstly, the precursors were loaded into a jar and mixed with 60 μL of deionized water. A ball milling process was then performed for 30 min at a speed of 600 rpm. The resulting product was subsequently dried in a vacuum-drying oven for 120 min at room temperature and annealed at 200 °C using a simple rapid thermal treatment (RTT) process. The RTT process was carried out on a rapid thermal processor, heating the sample to the annealing temperature at a rate of 10 °C s^{-1} . After remaining at the annealing temperature of 200 °C for 60–300 s, the system was rapidly cooled down to room temperature. Upon cooling to room temperature, the Mn^{2+} -doped CsSnCl_3 powder was obtained via ball milling for 30 min at a speed of 600 rpm. Figure 1 illustrates the Mn^{2+} -doped CsSnCl_3 synthesis process using water-assisted ball-milling at room temperature, followed by the RTT process. The crystal structures of Mn^{2+} -doped CsSnCl_3 were characterized using X-ray diffraction (XRD) (Bruker D8 Advance, Karlsruhe, Germany) at 35 kV and 35 mA. The compositions of the Mn^{2+} -doped CsSnCl_3 were analyzed through energy dispersive spectroscopy (EDS) (Bruker EDS QUANTAX, Karlsruhe, Germany). The structure of the Mn^{2+} -doped CsSnCl_3 sample (S- Mn^{2+} -doping) was characterized via scanning electron microscopy (SEM, Hitachi SU5000, Tokyo, Japan). PL measurements, including temperature-dependent PL spectra, PL excitation (PLE) spectra, and time-resolved PL spectra, were carried out using a PL spectrometer (FLS1000, Edinburgh Instrument, Livingstone, UK).

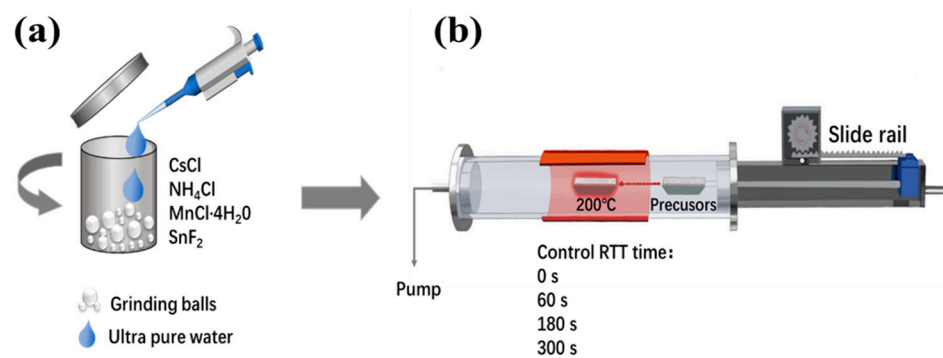


Figure 1. Schematic showing the method for (a) synthesizing Mn^{2+} -doped CsSnCl_3 and (b) RTT process.

3. Results and Discussion

Figure 2a displays the SEM image obtained from the Mn^{2+} -doped CsSnCl_3 powders prior to the RTT process. The EDS elemental mapping of the Mn^{2+} -doped CsSnCl_3 reveals a well-distributed presence of Cs, Pb, Cl, Mn, and F elements. Figure 2b indicates that the CsSnCl_3 powder retains a uniform distribution of Cs, Sn, Cl, Mn, and F elements even after the RTT process.

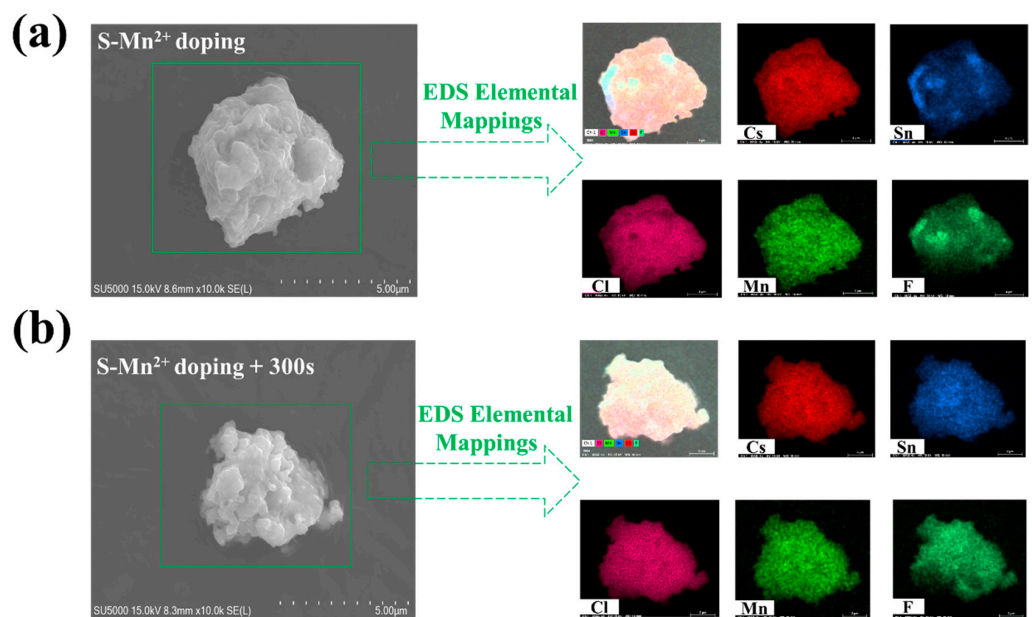


Figure 2. SEM image and EDS elemental maps of Cs, Sn, Mn, Cl, and F for a typical Mn^{2+} -doped CsSnCl_3 powder (a) before RTT process and (b) after RTT process for 300 s, respectively.

Figure 3a depicts the PL spectrum obtained from the Mn^{2+} -doped CsSnCl_3 powders prior to the RTT process. Pristine $\text{CsSnCl}_3:\text{Mn}^{2+}$ shows a double luminescence peak structure with PL peaks at ~ 450 nm and ~ 640 nm, respectively. As portrayed in the inset of Figure 3a, the 580 nm PL band from CsSnCl_3 powders without Mn^{2+} doping is due to the radiative recombination of self-localized excitons [21]. The addition of Mn^{2+} doping into CsSnCl_3 results in a significant 60 nm redshift in the PL, which is ascribed from the $4T^1 \rightarrow 6A^1$ transition of Mn^{2+} [22]. To comprehend the origin of the blue emission, the temperature-dependent PL spectra of the pristine $\text{CsSnCl}_3:\text{Mn}^{2+}$ were measured from 78 to 298 K. As illustrated in Figure 3b, the blue emission displayed an increase in PL intensity and a reduction in the full width at half maximum (FWHM) with decreasing temperature, which is due to thermal quenching. Nevertheless, its peak barely changes with temperature, suggesting a typical defect-related luminescence behavior and implying that the blue emission arises from the defect-related luminescence centers. In contrast, the red

emission intensity displays almost no recognizable changes with temperature, and only the PL peak redshifts slightly to 670 nm with decreasing temperature, indicating a competitive relationship between the blue and red emission in the pristine $\text{CsSnCl}_3:\text{Mn}^{2+}$. To clarify the PL characteristics, PL decay curves were measured under an excitation wavelength of 375 nm (375 nm, 70 ps excitation pulses LASER), portrayed in Figure 3c,d. The PL decay curve for blue emission was well-fitted with a biexponential decay function, while the PL decay curve for red emission was well-fitted with a triexponential decay function [23]:

$$I(t) = I_0 + A_1 \exp\left(\frac{-t}{\tau_1}\right) + A_2 \exp\left(\frac{-t}{\tau_2}\right) + A_3 \exp\left(\frac{-t}{\tau_3}\right) \quad (1)$$

where I_0 represents the background level; τ_1 , τ_2 , and τ_3 represent the lifetime of each exponential decay component, and A_1 , A_2 , and A_3 denote the corresponding amplitudes, respectively. Therefore, the intensity-weighted average PL lifetimes are determined using $(A_1 * \tau_1^2 + A_2 * \tau_2^2 + A_3 * \tau_3^2) / (A_1 * \tau_1 + A_2 * \tau_2 + A_3 * \tau_3)$ [24]. As demonstrated in Figure 3c, the blue emission exhibits a fast decay dynamic with a lifetime of 4.93 ns, while the red emission displays a slow decay behavior with a lifetime of 0.16 ms, which is five orders of magnitude longer than that of the blue emission. These findings adequately explain the competitive relationship between the defect-related luminescence centers and the Mn^{2+} state in the pristine $\text{CsSnCl}_3:\text{Mn}^{2+}$. Upon light excitation, the excitons lifted from the ground state to the excited state relax rapidly to the defect-related luminescence centers due to the fast decay dynamic, thereby significantly intensifying the blue emission.

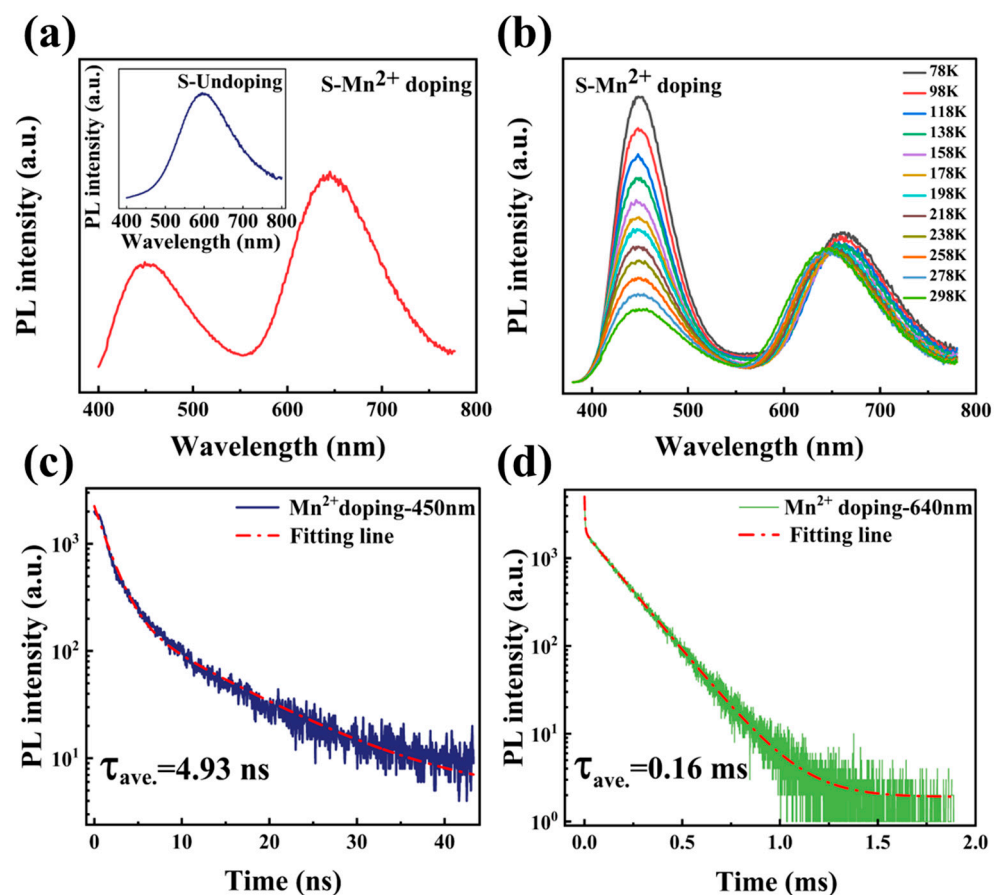


Figure 3. (a) PL spectrum from the Mn^{2+} -doped CsSnCl_3 powders without RTT process. Inset shows PL spectrum from the CsSnCl_3 powders. (b) Temperature-dependent PL spectra of the pristine $\text{CsSnCl}_3:\text{Mn}^{2+}$ measured in the range of 78 to 298 K. Time-resolved PL decay trace of (c) blue PL recorded at 450 nm and (d) red PL recorded at 640 nm in the pristine $\text{CsSnCl}_3:\text{Mn}^{2+}$.

The PL and PLE spectra of $\text{CsSnCl}_3:\text{Mn}^{2+}$ powders with and without the RTT process are depicted in Figure 4. Interestingly, it was observed that the RTT process led to a remarkable enhancement in red emission while significantly reducing the blue emission. Moreover, the intensity of the red emission increased with an increase in RTT time. Specifically, after the RTT process, the excitation peaks of $\text{CsSnCl}_3:\text{Mn}^{2+}$ at 355, 418, and 469 nm, corresponding to the ${}^6\text{A}_1({}^6\text{S}) \rightarrow {}^4\text{T}_2({}^4\text{D})$, ${}^4\text{T}_2({}^4\text{G})$, and ${}^4\text{T}_1({}^4\text{G})$ transitions of the Mn^{2+} ion [25], respectively, were observed, as shown in Figure 4. This strongly indicates that the RTT process effectively activates Mn^{2+} in CsSnCl_3 , leading to a significant enhancement in excited-state density, as revealed in Figure 4. Therefore, the enhancement in excited-state density is suggested to be responsible for the improved red emission. Interestingly, from Figure 4, it was found that the blue emission wavelength overlapped with the transition from ${}^6\text{A}_1({}^6\text{S}) \rightarrow {}^4\text{T}_2({}^4\text{G})$ and ${}^4\text{T}_1({}^4\text{G})$ of the Mn^{2+} ion. This indicates that the reduction in blue emission may have resulted from the energy transfer from the defect-related luminescent state to the ${}^6\text{A}_1({}^6\text{S}) \rightarrow {}^4\text{T}_2({}^4\text{G})$ and ${}^4\text{T}_1({}^4\text{G})$ transitions of the Mn^{2+} ion, which in turn contributes to the improvement in red PL intensity. Thus, the significant enhancement in red emission can be attributed to the enhanced excited-state density as well as energy transfer between the defect-related luminescent state and the Mn^{2+} state.

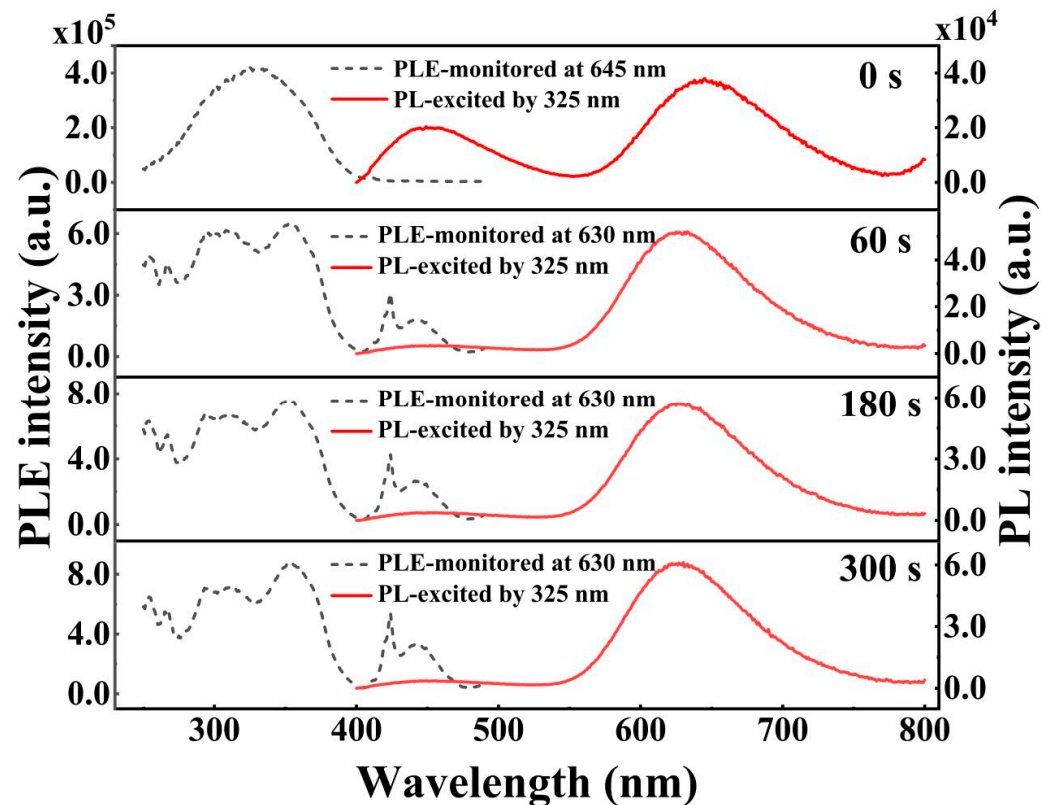


Figure 4. PL and PLE spectra of $\text{CsSnCl}_3:\text{Mn}^{2+}$ powders with and without RTT process, respectively.

Figure 5 presents the PL decay curves of the $\text{CsSnCl}_3:\text{Mn}^{2+}$ powders with and without the RTT process. It was found that the average lifetime rapidly increased from 0.16 ms to 4.73 ms after the RTT process. Furthermore, with an increase in the RTT processing time from 60 s to 300 s, the average lifetime gradually increased from 4.73 ms to 6.81 ms, indicating a reduction in nonradiative recombination centers. This was confirmed via the XRD patterns of the $\text{CsSnCl}_3:\text{Mn}^{2+}$ powders with and without the RTT process, as shown in Figure 6. For the $\text{CsSnCl}_3:\text{Mn}^{2+}$ powders without the RTT process, the diffraction peaks at 22.10° , 23.95° , 30.269° , and 31.142° corresponded to (400), (020), (411), and (002) crystal planes of cubic CsSnCl_3 (PDF# 71-2023), respectively. In addition, there were still small amounts of characteristic peaks of CsCl . However, after the RTT process, the

diffraction peaks corresponding to (400), (020), (411), and (002) crystal planes of cubic CsSnCl_3 became stronger and sharper with an increase in the RTT time from 60 s to 300 s. This strongly indicates an improved crystallinity of the $\text{CsSnCl}_3:\text{Mn}^{2+}$ powders after the RTT process, which coincided well with the increasing lifetime with an increase in the RTT time. Evidently, the RTT not only effectively activated the Mn^{2+} but also improved the crystallinity of the $\text{CsSnCl}_3:\text{Mn}^{2+}$ powders, thus reducing the nonradiative recombination centers and contributing to the enhancement in red emission. Raman spectra in Figure 7 show an array of symmetric ($125\text{--}175\text{ cm}^{-1}$) and asymmetric ($185\text{--}260\text{ cm}^{-1}$) stretching peaks for the SnCl_3^- group, and a peak at $\sim 275\text{ cm}^{-1}$, attributable to symmetric Mn–Cl stretching.

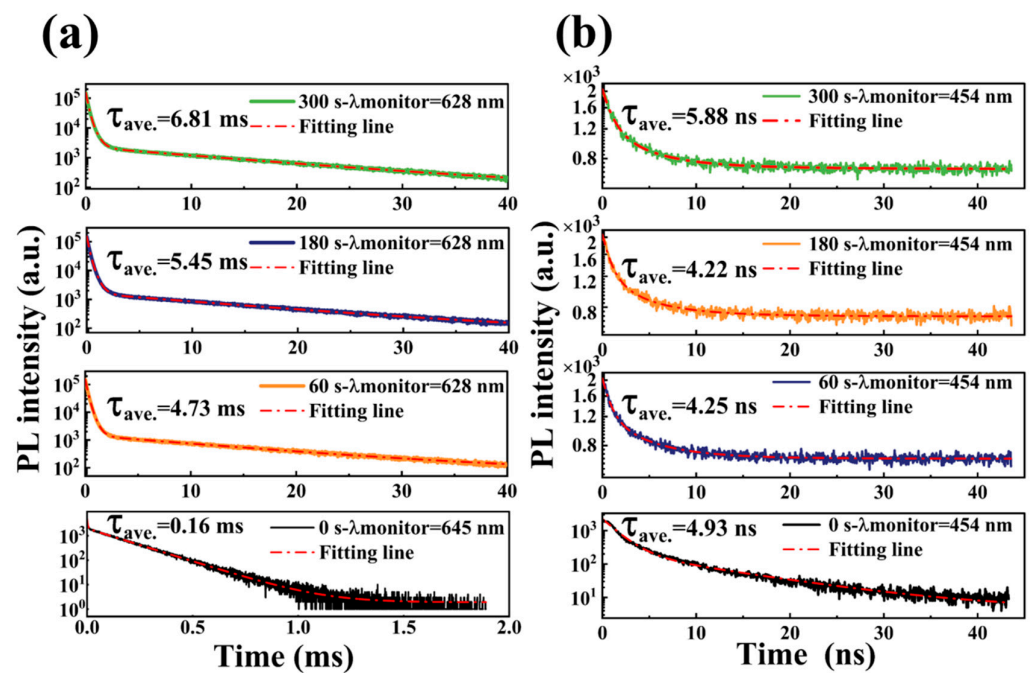


Figure 5. Time-resolved PL decay trace of (a) red PL recorded at corresponding PL peak and (b) blue PL recorded at 454 nm in the $\text{CsSnCl}_3:\text{Mn}^{2+}$ powders with and without RTT process, measured under an excitation wavelength of 375 nm (375 nm, 70 ps excitation pulses LASER).

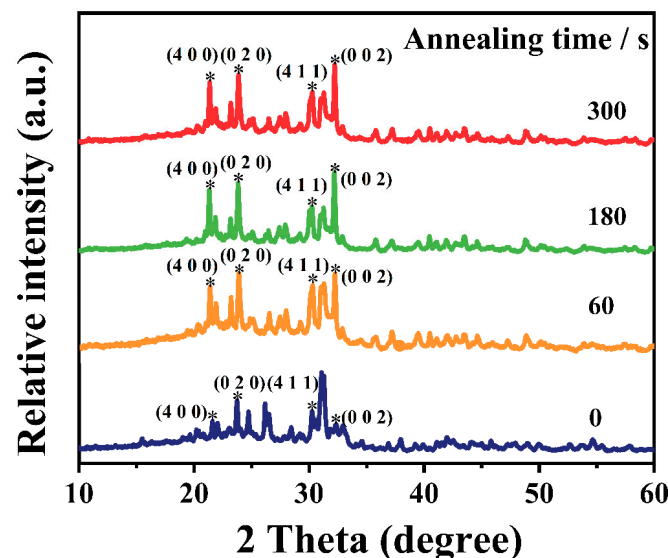


Figure 6. XRD patterns obtained for the $\text{CsSnCl}_3:\text{Mn}^{2+}$ powders with and without RTT process, The symbol “*” represents the corresponding crystal plane.

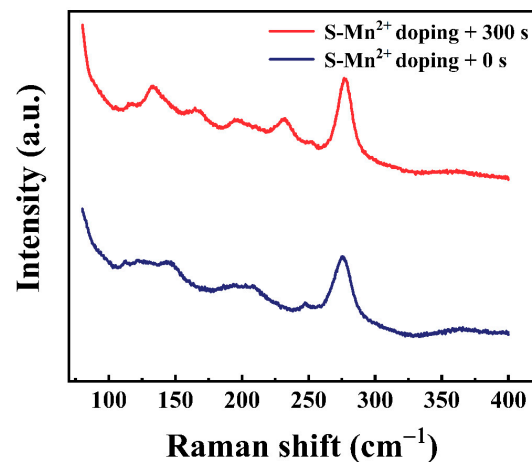


Figure 7. Raman spectra of $\text{CsSnCl}_3:\text{Mn}^{2+}$ powders with and without RTT process.

To gain a deeper understanding of the PL characteristics, the temperature-dependent PL spectra of the $\text{CsSnCl}_3:\text{Mn}^{2+}$ powders with 300 s of RTT processing were measured, and the results are shown in Figure 8. It was observed that with a decrease in temperature, there was a significant increase in the red PL intensity along with a slight increase in the blue PL intensity. This is in contrast to the behavior observed in the $\text{CsSnCl}_3:\text{Mn}^{2+}$ powders without the RTT process, as shown in Figure 3b. This increase can be attributed to the energy transfer from the defect-related luminescent state to the $6A^1(6S) \rightarrow 4T^2(4G)$ and $4T^1(4G)$ transitions of the Mn^{2+} ion. The temperature dependence of the integrated red PL intensity $I_{\text{PL}}(T)$ can be fitted using the Arrhenius equation given below [22]:

$$I_{\text{PL}}(T) = \frac{I_{\text{PL}}(T_0)}{1 + \beta \exp(-E_b/k_B T)} \quad (2)$$

where $I_{\text{PL}}(T_0)$ is the integrated PL intensity at 10 K, β is a constant related to the density of radiative recombination centers, k_B is Boltzmann's constant, and E_b is the exciton binding energy. Using this equation, the exciton binding energy E_b was empirically derived to be 31.6 meV, as shown in the inset of Figure 8. This further confirms that the red emission is from the Mn^{2+} state rather than from self-trapped excitons.

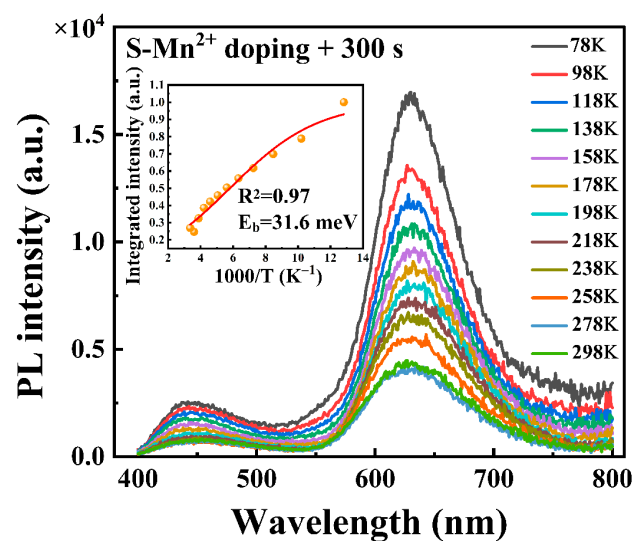


Figure 8. Temperature-dependent PL spectra of the $\text{CsSnCl}_3:\text{Mn}^{2+}$ powders with RTT processing for 300 s measured in the range of 78 to 298 K. Inset shows the integrated red PL intensities at different temperatures (orange solid symbols) and the fitting of the experimental data (red curve).

To evaluate the thermal stability of the $\text{CsSnCl}_3:\text{Mn}^{2+}$ powders, the temperature-dependent integrated PL intensities were monitored during thermal recycling. As shown in Figure 9, both samples experienced thermal quenching of PL as temperatures were increased from 25 to 165 °C. However, for pure CsSnCl_3 powders, a reduction of over 90% in PL intensity was observed after the heating and cooling cycles. In contrast, $\text{CsSnCl}_3:\text{Mn}^{2+}$ powders with RTT processing showed a slight enhancement in PL intensity after the heating and cooling cycles. Clearly, the $\text{CsSnCl}_3:\text{Mn}^{2+}$ powders with RTT processing displayed superior thermal and structural stability.

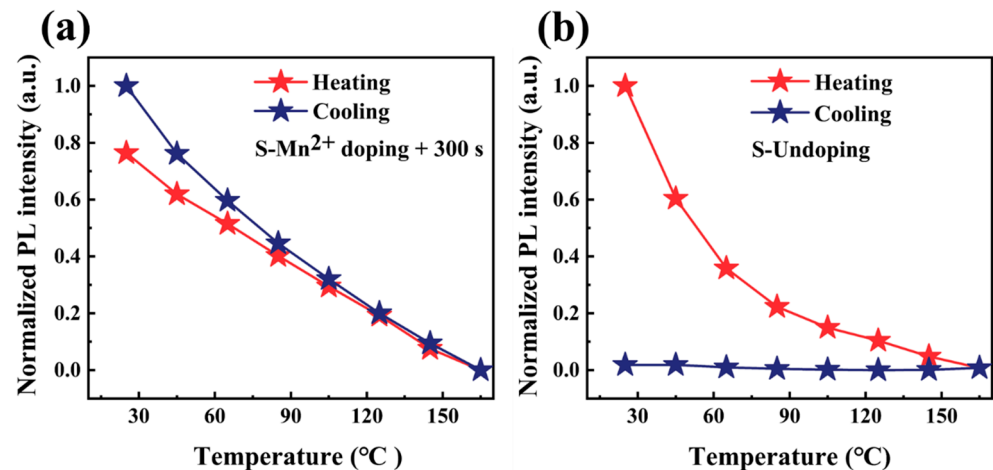


Figure 9. Heating and cooling cycling measurements at various temperatures: (a) pure CsSnCl_3 ; (b) $\text{CsSnCl}_3:\text{Mn}^{2+}$ powers with RTT processing for 300 s.

4. Conclusions

We demonstrated a rapid synthesis method for SnF_2 -derived $\text{CsSnCl}_3:\text{Mn}^{2+}$ perovskite and investigated the effect of RTT on its PL properties. We observed that pristine $\text{CsSnCl}_3:\text{Mn}^{2+}$ exhibited a double luminescence peak structure, attributed to defect-related luminescent centers and the $4T^1 \rightarrow 6A^1$ transition of Mn^{2+} . RTT was found to significantly reduce the blue emission and enhance the red emission intensity almost twofold compared to the pristine sample. This improvement in PL was suggested to arise from increased excited-state density, energy transfer between the defect-related state and the Mn^{2+} state, as well as a reduction of nonradiative recombination centers. Furthermore, we demonstrated that the Mn^{2+} -doped samples after RTT exhibit excellent thermal stability. Our findings clearly demonstrate that RTT not only can avoid thermal decomposition of tin-based halide perovskite materials during the heating process but also improve the crystallinity of $\text{CsSnCl}_3:\text{Mn}^{2+}$ powders, and more importantly provides an alternative method for thermal activation of the Mn ion luminescence center of tin-based perovskite, which has implications for the future development of optoelectronic devices.

Author Contributions: J.X.: investigation, formal analysis, and writing—original draft. H.W.: investigation, formal analysis. X.L.: investigation, and formal analysis. Y.H.: investigation, formal analysis. J.C.: investigation, formal analysis. W.Z.: investigation, formal analysis. Z.L.: investigation, formal analysis. J.S.: investigation, formal analysis. H.L.: formal analysis and writing—review and editing. R.H.: writing—review and editing, formal analysis, and funding acquisition. All authors have read and agreed to the published version of the manuscript.

Funding: This research was funded by the Guangdong Basic and Applied Basic Research Foundation (Grant Nos. 2020A1515010432), Project of Guangdong Province Key Discipline Scientific Research Level Improvement (Grant Nos. 2021ZDJS039, 2022ZDJS067), Special Innovation Projects of Guangdong Provincial Department of Education (Grant Nos. 2019KTSCX096, 2020KTSCX076), and the Special Fund for Science and Technology Innovation Strategy of Guangdong Province (Grant Nos. pdjh2023a0336).

Institutional Review Board Statement: Not applicable.

Informed Consent Statement: Not applicable.

Data Availability Statement: Data underlying the results presented in this paper are not publicly available at this time but may be obtained from the authors upon reasonable request.

Conflicts of Interest: The authors declare no conflict of interest.

References

1. Protesescu, L.; Yakunin, S.; Bodnarchuk, M.I.; Krieg, F.; Caputo, R.; Hendon, C.H.; Yang, R.X.; Walsh, A.; Kovalenko, M.V. Nanocrystals of cesium lead halide perovskites (CsPbX_3 , $X = \text{Cl}$, Br , and I): Novel optoelectronic materials showing bright emission with wide color gamut. *Nano Lett.* **2015**, *15*, 3692–3696. [[CrossRef](#)] [[PubMed](#)]
2. Li, X.; Wu, Y.; Zhang, S.; Cai, B.; Gu, Y.; Song, J.; Zeng, H. CsPbX_3 quantum dots for lighting and displays: Room-temperature synthesis, photoluminescence superiorities, underlying origins and white light-emitting diodes. *Adv. Funct. Mater.* **2016**, *26*, 2435–2445. [[CrossRef](#)]
3. Lin, K.; Xing, J.; Quan, L.N.; Arquer, F.P.G.; Gong, X.W.; Lu, J.X.; Xie, L.Q.; Zhao, W.; Zhang, J.D.; Yan, C.Z.; et al. Perovskite light-emitting diodes with external quantum efficiency exceeding 20 percent. *Nature* **2018**, *562*, 245–248. [[CrossRef](#)]
4. Liu, M.; Wan, Q.; Wang, H.; Carulli, F.; Sun, X.; Zheng, W.; Kong, L.; Zhang, Q.; Zhang, C.; Zhang, Q.; et al. Suppression of temperature quenching in perovskite nanocrystals for efficient and thermally stable light-emitting diodes. *Nat. Photonics* **2021**, *15*, 379–385. [[CrossRef](#)]
5. Fan, Q.; Biesold-McGee, G.V.; Ma, J.; Xu, Q.; Pan, S.; Peng, J.; Lin, Z. Lead-free halide perovskite nanocrystals: Crystal structures, synthesis, stabilities, and optical properties. *Angew. Chem. Int. Ed.* **2020**, *59*, 1030–1046. [[CrossRef](#)] [[PubMed](#)]
6. Li, X.; Gao, X.; Zhang, X.; Shen, X.; Lu, M.; Wu, J.; Shi, Z.; Colvin, V.L.; Hu, J.; Bai, X.; et al. Lead-Free Halide Perovskites for Light Emission: Recent Advances and Perspectives. *Adv. Sci.* **2021**, *8*, 2003334. [[CrossRef](#)]
7. Jing, Y.; Liu, Y.; Zhao, J.; Xia, Z. Sb^{3+} doping-induced triplet self-trapped excitons emission in lead-free Cs_2SnCl_6 nanocrystals. *J. Phys. Chem. Lett.* **2019**, *10*, 7439–7444. [[CrossRef](#)]
8. Lian, L.; Zheng, M.; Zhang, W.; Yin, L.; Du, X.; Zhang, P.; Zhang, X.; Gao, J.; Zhang, D.; Gao, L.; et al. Efficient and reabsorption-free radioluminescence in $\text{Cs}_3\text{Cu}_2\text{I}_5$ nanocrystals with self-trapped excitons. *Adv. Sci.* **2020**, *7*, 2000195. [[CrossRef](#)]
9. Cong, M.; Zhang, Q.; Yang, B.; Chen, J.; Xiao, J.; Zheng, D.; Zheng, T.; Zhang, R.; Qing, G.; Zhang, C.; et al. Bright triplet self-trapped excitons to dopant energy transfer in halide double-perovskite nanocrystals. *Nano Lett.* **2021**, *21*, 8671–8678. [[CrossRef](#)]
10. Su, B.; Jin, J.; Peng, Y.; Molokeev, M.S.; Yang, X.; Xia, Z. Zero-Dimensional Organic Copper(I) Iodide Hybrid with High Anti-Water Stability for Blue-Light-Excitable Solid-State Lighting. *Adv. Opt. Mater.* **2022**, *10*, 2102619. [[CrossRef](#)]
11. Jellicoe, T.C.; Richter, J.M.; Glass, H.F.J.; Tabachnyk, M.; Brady, R.; Dutton, S.E.; Rao, A.; Friend, R.H.; Credgington, D.; Greenham, N.C.; et al. Synthesis and optical properties of lead-free cesium tin halide perovskite nanocrystals. *J. Am. Chem. Soc.* **2016**, *138*, 2941–2944. [[CrossRef](#)]
12. Liu, Q.; Yin, J.; Zhang, B.-B.; Chen, J.-K.; Zhou, Y.; Zhang, L.-M.; Wang, L.-M.; Zhao, Q.; Hou, J.; Shu, J.; et al. Theory-guided synthesis of highly luminescent colloidal cesium tin halide perovskite nanocrystals. *J. Am. Chem. Soc.* **2021**, *143*, 5470–5480. [[CrossRef](#)]
13. Chiara, R.; Ciftci, Y.O.; Queloz, V.I.E.; Nazeeruddin, M.K.; Grancini, G.; Malavasi, L. Green-emitting lead-free Cs_4SnBr_6 zero-dimensional perovskite nanocrystals with improved air stability. *J. Phys. Chem. Lett.* **2020**, *11*, 618–623. [[CrossRef](#)] [[PubMed](#)]
14. Benin, B.M.; Dirin, D.N.; Morad, V.; Wörle, M.; Yakunin, S.; Rainò, G.; Nazarenko, O.; Fischer, M.; Infante, I.; Kovalenko, M.V. Highly emissive self-trapped excitons in fully inorganic zero-dimensional tin halides. *Angew. Chem. Int. Ed.* **2018**, *57*, 11329–11333. [[CrossRef](#)] [[PubMed](#)]
15. Zhang, X.; Wang, H.; Wang, S.; Hu, Y.; Liu, X.; Shi, Z.; Colvin, V.L.; Wang, S.; Yu, W.W.; Zhang, Y. Room temperature synthesis of all inorganic lead-free zero-dimensional Cs_4SnBr_6 and $\text{Cs}_3\text{KSnBr}_6$ perovskites. *Inorg. Chem.* **2019**, *59*, 533–538. [[CrossRef](#)] [[PubMed](#)]
16. Tan, L.; Wang, W.; Li, Q.; Luo, Z.; Zou, C.; Tang, M.; Zhang, L.; He, J.; Quan, Z. Colloidal syntheses of zero-dimensional Cs_4SnX_6 ($X = \text{Br}$, I) nanocrystals with high emission efficiencies. *Chem. Commun.* **2020**, *56*, 387–390. [[CrossRef](#)]
17. Xu, K.; Wei, Q.; Wang, H.; Yao, B.; Zhou, W.; Gao, R.; Chen, H.; Li, H.; Wang, J.; Ning, Z. The 3D-structure-mediated growth of zero-dimensional Cs_4SnX_6 nanocrystals. *Nanoscale* **2022**, *14*, 2248–2255. [[CrossRef](#)]
18. Zhang, Q.; Liu, S.; He, M.; Zheng, W.; Wan, Q.; Liu, M.; Liao, X.; Zhan, W.; Yuan, C.; Liu, J.; et al. Stable lead-free tin halide perovskite with operational stability >1200 h by suppressing Tin(II) oxidation. *Angew. Chem. Int. Ed.* **2022**, *61*, e202205463.
19. Dawson, M.; Ribeiro, C.; Morelli, M.R. MnCl_2 doping increases phase stability of tin halide perovskites. *Mater. Sci. Semicond. Process.* **2021**, *132*, 105908. [[CrossRef](#)]
20. Hou, L.; Zhu, Y.; Zhu, J.; Gong, Y.; Li, C. Mn-doped 2D Sn-based perovskites with energy transfer from self-trapped excitons to dopants for warm white light-emitting diodes. *J. Mater. Chem. C* **2020**, *8*, 8502–8506. [[CrossRef](#)]
21. Voloshinovskii, A.S.; Myagkota, S.V.; Pidzyrailo, N.S.; Tokarivskii, M.V. Luminescence and structural transformations of CsSnCl_3 Crystals. *J. Appl. Spectrosc.* **1994**, *60*, 226–228. [[CrossRef](#)]

22. Lin, Z.; Wang, A.; Huang, R.; Wu, H.; Song, J.; Lin, Z.; Hou, D.; Zhang, Z.; Guo, Y.; Lan, S. Manipulating the sublattice distortion induced by Mn²⁺ doping for boosting the emission characteristics of self-trapped excitons in Cs₄SnBr₆. *J. Mater. Chem. C* **2023**, *11*, 5680–5687. [[CrossRef](#)]
23. Lin, K.; Liou, S.; Chen, W.; Wu, C.; Lin, G.; Chang, Y. Tunable and stable UV-NIR photoluminescence from annealed SiO_x with Si nanoparticles. *Opt. Express* **2013**, *21*, 23416–23424. [[CrossRef](#)] [[PubMed](#)]
24. Lin, Z.; Lin, Z.; Guo, Y.; Wu, H.; Song, J.; Zhang, Y.; Zhang, W.; Li, H.; Hou, D.; Huang, R. Effect of a-SiC_xN_y:H encapsulation on the stability and photoluminescence property of CsPbBr₃ quantum dots. *Nanomaterials* **2023**, *13*, 1228. [[CrossRef](#)]
25. Liu, W.-R.; Chiu, Y.-C.; Yeh, Y.-T.; Jang, S.-M.; Chen, T.-M. Luminescence and Energy Transfer Mechanism in Ca₁₀K(PO₄)₇: Eu²⁺, Mn²⁺ Phosphor. *J. Electrochem. Soc.* **2009**, *156*, J165. [[CrossRef](#)]

Disclaimer/Publisher's Note: The statements, opinions and data contained in all publications are solely those of the individual author(s) and contributor(s) and not of MDPI and/or the editor(s). MDPI and/or the editor(s) disclaim responsibility for any injury to people or property resulting from any ideas, methods, instructions or products referred to in the content.